PNAS RESEARCH ARTICLE | BIOPHYSICS AND COMPUTATIONAL BIOLOGY

Deep learning reveals how cells pull, buckle, and navigate fibrous environments

Abinash Padhi[a,1], Arka Daw[b,1], Atharva Agashe[a], Medha Sawhney[b], Maahi M. Talukder[a], Mehran M. H. Pour[a], Mohammad Jafari[c], Guy M. Genin[d,e], Farid Alisafaei[c,2], Sohan Kale[a,f,2], Anuj Karpatne[b,2], and Amrinder S. Nain[a,f,2]

Affiliations are included on p. 11.

Edited by Herbert Levine, Northeastern University, Boston, MA; received November 26, 2024; accepted October 20, 2025

Cells in tissues navigate fibrous environments fundamentally differently than they do on flat substrates, but the establishment of cell forces in physiological fibrous settings remains poorly understood. Although factors such as the stiffness of the extracellular matrix (ECM) are known to drive behaviors, including cell motility on flat nonfibrous substrates, the interplay between fiber architecture and stiffness in fibrous ECM is not known. Here, we find that in fibrous environments, the directionality of mechanical forces overrides ECM stiffness as the primary regulator of contractility in migrating cells. Using an approach combining phase microscopy with deep learning to map forces in real time, termed deep learning-enabled live-cell fiber-force microscopy (DLFM), we reveal that when cells transition between anisotropic and isotropic stress fields, their contractility significantly drops despite encountering stiffer ECM, contrary to the behavior of cells on flat nonfibrous substrates. Unlike the peripheral adhesions observed on flat nonfibrous substrates, cells in fibrous matrices form force-generating adhesions throughout their body, stabilized by out-of-plane mechanical components unique to fiber geometry. Cells exhibit distinct force signatures during migration, division, and differentiation, with temporal signatures that predict stem cell fate. These findings, enabled by combining deep learning and the mechanics of cells and fibers, explain long-standing paradoxical behavior of cells navigating deformable fibrous environments, how they can pull and tug at them, and identify tension anisotropy as a master regulator of cell behavior, with implications for cancer invasion, tissue engineering, and regenerative medicine.

traction force microscopy | cell-fiber interactions | mechanobiology | focal adhesions | machine learning

Significance

The mechanical forces cells generate govern behaviors from embryonic development to cancer metastasis. Nearly all knowledge of these forces comes from cells on flat surfaces, environments that poorly represent the fibrous architecture of real tissues. We found that in fibrous environments, cells follow different mechanical rules: They form force-generating attachments throughout their body rather than just at edges, and they respond more strongly to the directionality of tension than to matrix stiffness. We develop nondisruptive, live-cell, and real-time measurement of forces exerted on fibers to uncover force signatures during migration and stem cell differentiation. These findings overturn conventional understanding of cellular mechanosensitivity, revealing principles that govern cell behavior in health and disease.

Cells generate mechanical forces to migrate, divide, and maintain tissue architecture in fibrous environments, but our understanding of these forces comes almost entirely from studies on flat, continuous substrates that bear little resemblance to the fibrous networks of living tissues (1–7). This disconnect has left fundamental questions unanswered, including how force dynamics relate to fiber architecture and stiffness in critical cellular decisions like differentiation, and how cells in three-dimensional (3D) matrices form adhesions in locations that would be unstable on two-dimensional (2D) surfaces. Addressing these questions has been impossible because existing methods require either killing cells, paralyzing them with drugs, or labeling them with fluorescent markers, all of which can alter the behaviors we seek to understand.

The challenge is particularly acute for understanding focal adhesions, the force-transmitting structures that connect cells to their surroundings. On flat substrates, these adhesions form exclusively at cell edges where shear forces stabilize them (8). However, cells in fibrous matrices display a fundamentally different pattern, with adhesions often appearing far from the cell periphery (9–18), which causes differences in force patterns. Traditional traction force microscopy (19–24), while being powerful for studying cells on continuous substrates, cannot resolve the mechanical interactions between living cells and individual fibers. Methods adapted for 3D hydrogels (25) provide spatial resolution but use materials that differ substantially from native fibrous ECM, while approaches for fibrous systems lack the resolution to track adhesion dynamics or require endpoint measurements that miss critical temporal information (9, 10, 18, 26–30).

The inability to measure forces in real time has obscured another fundamental aspect of cellular mechanics: How the directionality of mechanical signals influences cell behavior. Recent evidence suggests that differences in mechanical tension between directions ("tension anisotropy") may be as important as absolute stiffness in regulating cell fate (31). However, testing this hypothesis requires tracking forces continuously as cells navigate

Author contributions: A.S.N. conceived and supervised the study; A.P., G.M.G., F.A., S.K., A.K., and A.S.N. designed research; A.P., A.D., A.A., M.S., M.M.H.P., G.M.G., F.A., S.K., A.K., and A.S.N. performed research; A.P., A.D., A.A., M.S., M.M.T., M.M.H.P., M.J., G.M.G., F.A., S.K., A.K., and A.S.N. contributed new reagents/analytic tools; A.P., A.D., A.A., M.S., M.M.T., M.M.H.P., M.J., G.M.G., F.A., S.K., A.K., and A.S.N. analyzed data; and A.P., A.D., G.M.G., F.A., S.K., A.K., and A.S.N. wrote the paper.

The authors declare no competing interest.

This article is a PNAS Direct Submission.

[1]A.P. and A.D. contributed equally to this work.

[2]To whom correspondence may be addressed. Email: farid.alisafaei@njit.edu, kale@vt.edu, karpatne@vt.edu, or nain@vt.edu.

This article contains supporting information online at https://www.pnas.org/lookup/suppl/doi:10.1073/pnas.2424047122/-/DCSupplemental.

Published November 21, 2025.

between regions of different mechanical properties, something current methods cannot achieve.

To measure cellular forces in real time as cells migrate through fibrous matrices, we developed a method called deep learning-enabled live-cell fiber-force microscopy (DLFM). This technique uncovered principles of cellular mechanics. DLFM integrates standard phase-contrast microscopy with deep learning algorithms trained to simultaneously track both cells and fiber deformations, enabling continuous, label-free force measurements without chemical perturbations.

Developing DLFM involved addressing several key challenges. Most deep learning methods can track deformation on static backgrounds (32–36), but segmenting semitransparent, moving cells on a similarly deforming, fibrous background requires much higher resolution than previously available (37). Furthermore, conventional segmentation methods each have limitations: Deep learning-based segmentation requires large, annotated datasets (38); optical flow techniques struggle when both the foreground and background are semitransparent and deforming (39); active contour models perform poorly with partially transparent objects (40); and generative adversarial networks (GANs), though powerful, are computationally intensive and often unstable when modeling subtle transparency and deformation (41).

Physics-based models can simplify AI algorithms (42), but they are less effective when the underlying biophysical processes, such as those governing cell migration, are not well understood. However, prior work has shown that integrating phase-contrast microscopy with GANs can enhance image quality (43), and predict fluorescent labeling patterns in unlabeled cells (32, 44, 45). Based on this, we designed DLFM using a GAN architecture. Using a system of parallel labeled training image datasets, we sidestepped issues of cell translucency and simultaneous foreground and background deformation.

We developed the DLFM method using a well-defined crosshatch network of fibers, which allowed us to vary the interfiber spacing, thus achieving robust control on diverse cell shapes (30). The DLFM platform revealed three surprising findings that reshape our understanding of how cells interact with their mechanical environment. First, we found that tension anisotropy dominates over ECM stiffness in controlling cellular contractility (31). Cells migrating from anisotropic to isotropic stress fields reduced their forces, despite moving into regions of higher overall stiffness, in contrast to the prevailing view that stiffer environments always promote stronger cellular forces. Second, we found that out-of-plane mechanical components unique to fibrous geometries enable cells to form stable focal adhesions throughout their body, not just at their periphery. Integrated experiments and computational modeling demonstrated how these interior adhesions arise from the 3D nature of cell–fiber interactions. Finally, we resolve force signatures during migration, cell–cell interactions, and differentiation. These temporal dynamics, invisible to endpoint measurements, revealed that stem cells undergoing adipogenic differentiation suppress forces early, while those undergoing osteogenic differentiation enhance forces late, suggesting mechanical signatures of cell fate decisions. Together, these findings establish tension anisotropy as a master regulator of the interactions of migrating cells with fibrous networks and demonstrate how real-time force measurements can uncover biological principles hidden from traditional approaches.

Results

Nonuniform, Out-of-Plane Stresses Enable Adhesions to Form Away from the Cell Periphery. To understand how cells exert forces on their surroundings, we first examined how they form connections with the extracellular matrix (ECM). Cells generate forces through focal adhesions, molecular assemblies that physically anchor the cell to the ECM. While previous studies using flat surfaces (2D nonfibrous hydrogels) showed that these adhesions form primarily at the cell edge, a fundamentally different pattern emerged in our fibrous environments. These were evident in human mesenchymal stem cells (hMSCs) on networks of orthogonal fibers, which, unlike flat nonfibrous 2D substrates, exhibited focal adhesions distributed across the entire cell surface, including regions far from the cell periphery (Fig. 1 *A* and *B*).

We used a chemomechanical cell model to investigate the mechanisms behind this distinct focal adhesion formation in fibrous ECMs, previously validated on 2D nonfibrous ECMs (*SI Appendix*, Fig. S1) (46). The model incorporates key cytoskeletal components involved in adhesion, including myosin, actin, microtubules, and focal adhesions (*SI Appendix*, *Notes* 1 and 2 and *Materials and Methods*). Central to the model is the hypothesis that actomyosin contractility and focal adhesion formation are regulated by mechanical tension generated within the cytoskeleton and at the cell–ECM interface, respectively.

Simulations began with two initial conditions: i) uniform and isotropic cell contraction, reflecting a uniform initial distribution of myosin and actin densities, both spatially and in terms of orientation distribution, and ii) a uniform, compliant layer of focal adhesions, modeling immature adhesions and weak cell–ECM connections (Fig. 1*C*). Starting from these conditions, the model predicted that cell contraction would stretch immature focal adhesions (Fig. 1*C*). Prolonged stretching matured the adhesions to a stiffer state, creating a stronger link between the cell and ECM that resisted further contraction and upregulated cytoskeletal tension. This tension promoted actomyosin contractility (47), stiffening actin along the direction of maximum principal stress and representing actin filament formation (Fig. 1*C*), matching experiments on aligned fibers (18).

Consistent with our experimental observations on crosshatch networks, the simulations showed that mature focal adhesions were not limited to the cell periphery and could form at a considerable distance from the cell periphery along nanofibers (Fig. 1 *D* and *E* and Movie M1). The model revealed that the formation of these nonperipheral focal adhesions was regulated by out-of-plane stresses exerted on nanofibers. Suppressing this by restricting cells to 2D nonfibrous ECM or by allowing only in-plane stresses at the cell–fiber interface in the simulations caused focal adhesions to organize to the cell periphery (*SI Appendix*, Fig. S2), as seen on traditional 2D nonfibrous substrates (46, 48, 49). The existence of out-of-plane, cell-generated forces on 2D planar hydrogels has been previously demonstrated using 2.5D traction force microscopy, which revealed upward and downward tractions localized around focal adhesions near the cell edge, generating rotational moments at the periphery (50). However, here we show that such out-of-plane forces can arise at locations far from the cell periphery in fibrous environments and regulate the formation of focal adhesions in these nonperipheral regions. This behavior is not observed on classical 2D hydrogels, where out-of-plane forces and focal adhesions remain confined to peripheral zones, as we showed in *SI Appendix*, Fig. S2 and consistent with previous findings (50).

The model also predicted that actin fibers would form in the directions of maximum principal stress. We found close agreement between predicted orientations and experimental images (Fig. 1 *D* and *E* and *SI Appendix*, Figs. S3 and S4), further validating the model and supporting our hypothesis on the central role of mechanical tension in directing cell–ECM interactions. However, our simulations demonstrated that mechanical stress (and consequently, the formation of focal adhesions and actin networks) is highly dynamic,

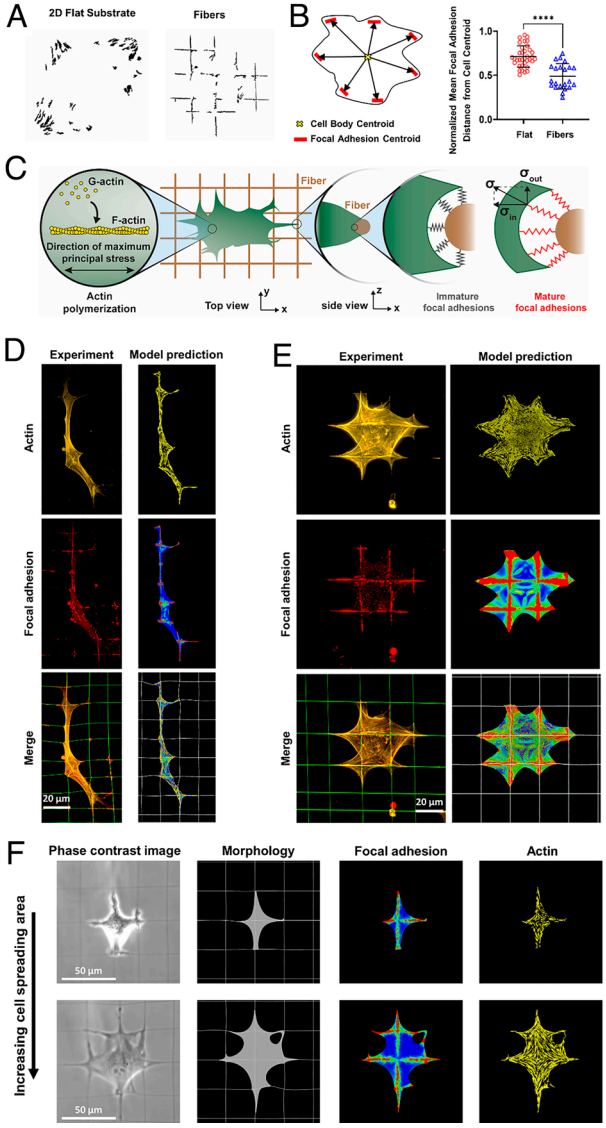

Fig. 1. Tensile stresses generated within the cytoskeleton and at the cell–matrix interface regulate the formation of actomyosin structures and mature focal adhesions. (*A* and *B*) By staining focal adhesions with paxillin, we observed that unlike cells cultured on 2D flat substrates, where mature focal adhesions were primarily localized at the cell periphery, cells cultured on networks of orthogonal fibers exhibited focal adhesions distributed throughout the entire cell surface, including regions distant from the cell edges. (*C*) Using an active contractile cell model, we simulated cell contraction on crosshatch fiber networks. Simulations began with two initial conditions: i) uniform, isotropic cell contraction, with a uniform distribution of myosin and actin densities throughout the cell in all directions, and ii) a uniform and compliant layer of immature focal adhesions with weak cell–fiber connections. After that, cell contraction generated nonuniform tension within the cytoskeleton and at the cell–matrix interface, depending on cell morphology and spreading, promoting actomyosin expression and actin fiber formation in the direction of maximum principal cytoskeletal stress. Tension at the cell–fiber interface matured focal adhesions connecting the cell to the fibers. (*D* and *E*) Simulation results for two representative cells, one elongated and one well-spread. The *Top* panels depict the direction of maximum principal stress in the cytoskeleton, indicating the orientation of actin fiber formation in the model. The middle panels show a heatmap of maximum principal stress at the cell–fiber interface, demonstrating the formation of mature focal adhesions in the model. Model predictions for the formation of actin and focal adhesions were validated against staining for actin (phalloidin) and paxillin, respectively. These results confirmed that actin forms along the direction of maximum principal stress, and unlike focal adhesions on 2D hydrogels, which typically form at the cell periphery, focal adhesions in fibrous networks can also form at locations distant from the cell edge. Notably, the mechanical stresses generated by cell contraction regulate both actin organization and focal adhesion formation. (*F*) Our model showed that these mechanical stresses and, consequently, the formation of focal adhesions and actin networks, are highly dynamic, changing significantly as cells alter their spreading area and shape.

changing continuously as cells adjust their spreading area and shape during migration (Fig. 1*F*). However, no existing approach allows for real-time measurement of cell-generated stress on fibrous ECMs. This limitation motivated us to develop a real-time technique to measure cell traction forces in fibrous matrices.

Estimation of Cellular Forces from Phase Contrast Images. The initial step in quantifying cellular forces requires measuring the deformation of ECM fibers induced by cell-generated forces. To resolve deformations of an initially orthogonal fiber network with hMSCs migrating on it, we developed a conditional generative adversarial network (cGAN) deep learning model for reconstituting fiber geometry from phase contrast images (Fig. 2*A* and Movies M2 and M3). We developed a "pix2pix" cGAN to resolve the fiber deformations by training the model on paired phase contrast and fluorescence microscopy images of cells deforming fluorescently labeled fibers (51–53) (Figs. 2 *B*, *i* and 3 *A*, *i*). Phase contrast images of fibers were obscured by cells, but fluorescence images were not (Fig. 2 *A*, *i* and *ii*). The cGAN's generator, $G: x \rightarrow y$, was trained to map a phase contrast input image x to a fluorescence image y. The cGAN's discriminator, D, was trained to distinguish between real images y and reconstituted images $G(x)$. After training the cGAN on a manually curated dataset (*SI Appendix, Note* 3), it robustly reconstituted fluorescent images of deformed fiber networks from experimental phase-contrast images (Fig. 3 *A*, *ii* and Movies M4 and M5).

These reconstituted images were analyzed to identify fiber intersection "nodes" (red dots, Fig. 3 *B*, *i*) and to track them across frames (Fig. 2 *B*, *ii*) using the deep learning–based object detection model *RetinaNet* (54). To improve accuracy, we developed a bidirectional tracking algorithm. For each timeframe t_i, a cross-correlation based forward nodal tracking algorithm (Fig. 3 *B*, *ii*) was used to estimate nodal mapping using positions from the previous timeframe t_{i-1}. Candidate cross-correlated nodes were combined with nodes detected by *RetinaNet* using a matching algorithm (*SI Appendix,* Fig. S5) that mapped intersections from t_{i-1} to t_i. This was repeated to map intersections from t_{i+1} back to t_i, resulting in a complete bidirectional tracking algorithm (Fig. 3 *B*, *iii*; see *Materials and Methods* for details). Nodal positions were then used to calculate fiber deformations, which showed a decrease in displacement away from the cell body (*SI Appendix,* Figs. S6 and S7). An inverse problem was solved to estimate force fields from these fiber deformations (Fig. 2*C*). These analyses, shown in *SI Appendix,* Figs. S6 and S7, examine how displacement magnitudes (u) decay with distance (δ) from the center of the force pattern. The displacement field generated by a simple force dipole shown in *SI Appendix,* Fig. S6*A* exhibits the characteristic features of the decay response observed in all cases. For small δ, below about 3 times the dipole separation, the slower decay is characterized by $u \sim \delta^{-\alpha}$ with $\alpha < 1$. Whereas for large δ, the decay is faster with α between 1 and 2, depending on the measurement direction. Similar trends are observed for simulated quadrupole (*SI Appendix,* Fig. S6*B*) and representative experimental examples (*SI Appendix*, Fig. S7). Overall, due to the sparse architecture of our nanofiber networks, the deformation decay is much slower when compared to thick 2D or 3D linear gels (3, 10, 55, 56), especially for smaller δ.

To assess the effectiveness of node tracking, we analyzed synthetically generated images. Precision and recall (57) were computed, with precision defined as the ratio of the number of correctly identified nodes to the total number of nodes identified and recall defined as the ratio of the number of nodes correctly identified to the actual number of nodes (ground truth). Precision and recall were both near the ideal value of 1 for seventeen videos

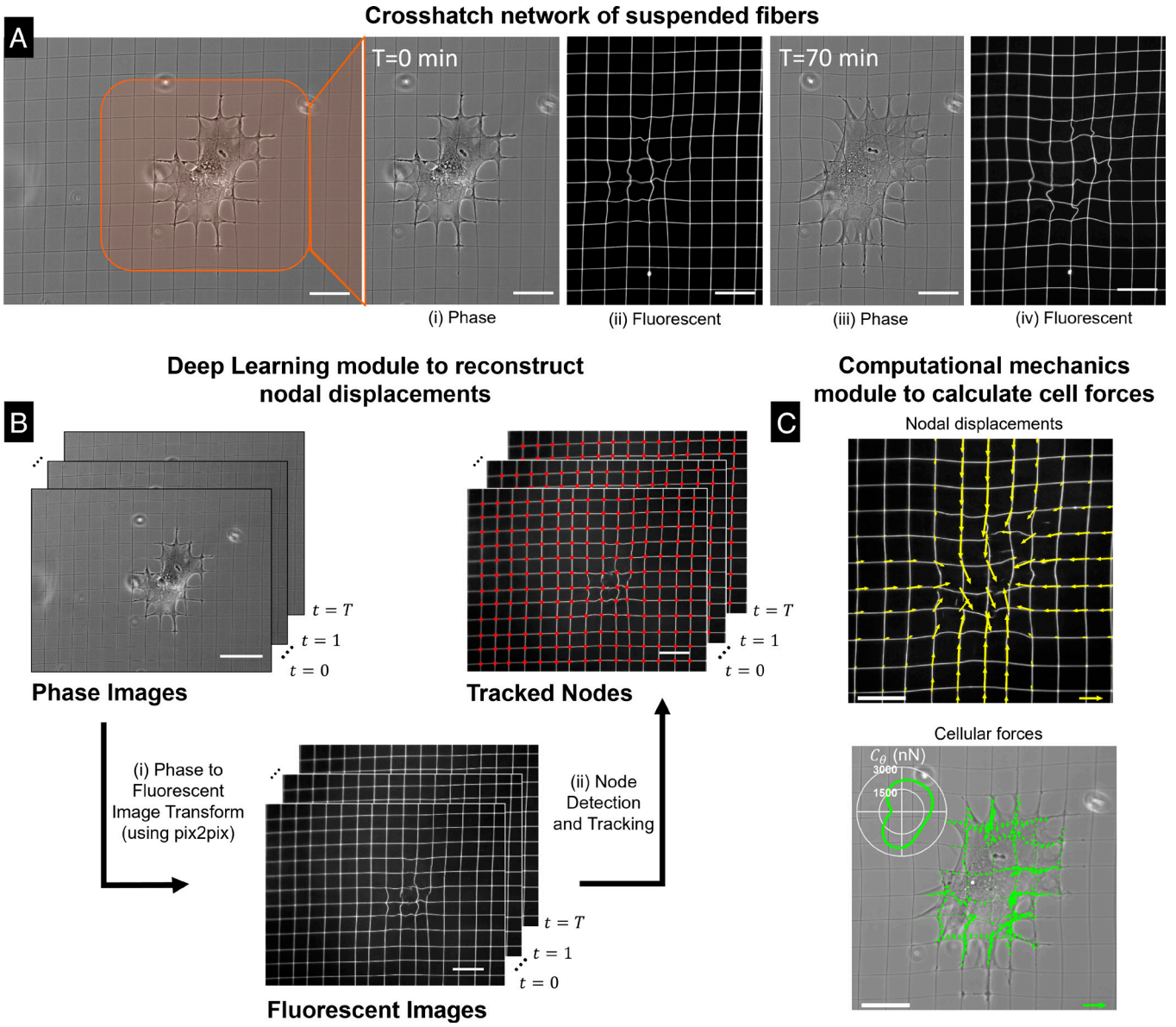

Fig. 2. Cell force computation algorithm. (*A*) Cells migrate over suspended crosshatch fiber networks, deforming the underlying fiber network, as seen in experimentally obtained phase-contrast (*i* and *iii*) and corresponding fluorescence microscopy images (*ii* and *iv*). Experimental fluorescent images were used exclusively to train the deep learning modules. (*B*) (*i*) Phase contrast images were transformed into synthetically generated fluorescent images through a deep learning–based model (pix2pix). (*ii*) A deep learning–based object detection model, RetinaNet, and a bidirectional tracking algorithm identified nodal intersection points of the fiber network (red dots added for visualization). (*C*) Displacement fields were calculated using the extracted nodal points (yellow arrows). Cell forces computed from displacement fields were represented as line tension (green arrows). Force polarity maps (C_θ, *Inset*) captured the orientational distribution of cellular forces. (Scale bar: 50 μm, Yellow arrow: 5 μm, Green arrow: 35 mN/m).

analyzed (Fig. 3 *B*, *iv*), demonstrating accurate node detection and tracking.

The spatial accuracy of node tracking, defined as the average root mean squared error (RMSE) of the Euclidean distance between experimentally estimated and ground truth node positions (Fig. 3 *B*, *v*), was below 2 pixels, on the order of expected human measurement error (*SI Appendix*, Fig. S8). RMSE was relatively small for nodes with a high "Node Detection" confidence score (>0.7) generated by *RetinaNet* and the RMSE across all 44,852 detected nodes (Fig. 3 *B*, *vi*), prompting us to eliminate detected nodes with a confidence score less than 0.7 in subsequent analyses.

We needed a reference map of where the fibers would be without any cell-generated forces to calculate how much cells deformed the fibers. We created this reference map by taking advantage of the precise geometric pattern of our crosshatch fiber networks (*SI Appendix*, Fig. S9 and *Note* 4). This represents a key advantage over traditional force measurement methods, which require adding drugs to temporarily paralyze cells to obtain such reference measurements.

Estimation of Forces by an Inverse Mechanics Formulation. We developed an inverse formulation to infer forces from the nodal displacements and deformed fiber shapes (*Materials and Methods*). To validate this and test its accuracy, we generated nodal displacement data ($\mathbf{u}_m$) at grid intersections by applying representative force patterns to a computational model of the crosshatch fiber network (red arrows, Fig. 4*A*) and simulated measurement errors (*SI Appendix*, Fig. S8) by adding zero-mean Gaussian noise of varying strength (σ_e = {0.0 μm, 0.1 μm, 0.2 μm, 0.5 μm}) to $\mathbf{u}_m$. An example of the recovered force pattern obtained by solving the regularized inverse problem for σ_e = 0.2 μm

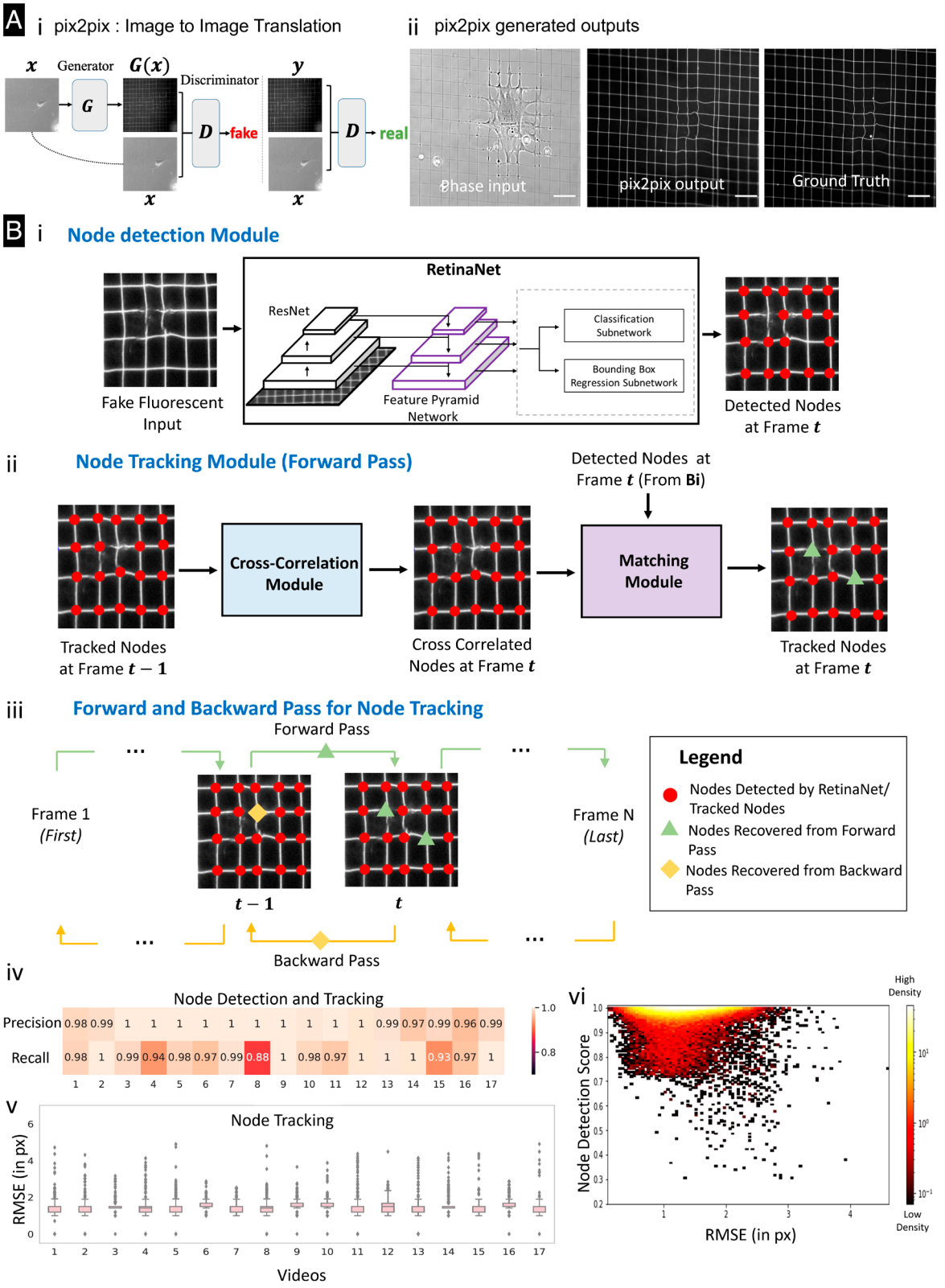

Fig. 3. Deep learning–based image reconstruction and feature extraction. (*A*) (*i*) Schematic representation of our pix2pix model, which generates fluorescent images from input phase-contrast experimental images. (*ii*) An example of a synthetically generated fluorescent image obtained from a trained pix2pix model. (Scale bar: 50 μm.) (*B*) (*i*) Node Detection Module that uses a deep learning–based object detection model called *RetinaNet* to identify grid intersections/nodes from synthetically generated fluorescent images. (*ii*) An illustration of the forward pass of the node tracking algorithm, (*iii*) A schematic representation of the forward and backward passes of the proposed bidirectional Tracking algorithm, (*iv*) *Precision* and *Recall* values of the predicted nodes after node detection and tracking are close to ~1 across all 17 videos, indicating close to ideal performance. (*v*) The distribution of Nodal Errors observed after node detection and tracking in each video shows that the average nodal error is less than 2 pixels, comparable to human measurement error. (*vi*) The scatter plot of node detection confidence scores vs nodal errors shows high confidence (greater than 0.7) of the RetinaNet for most of the predicted nodes with low nodal errors.

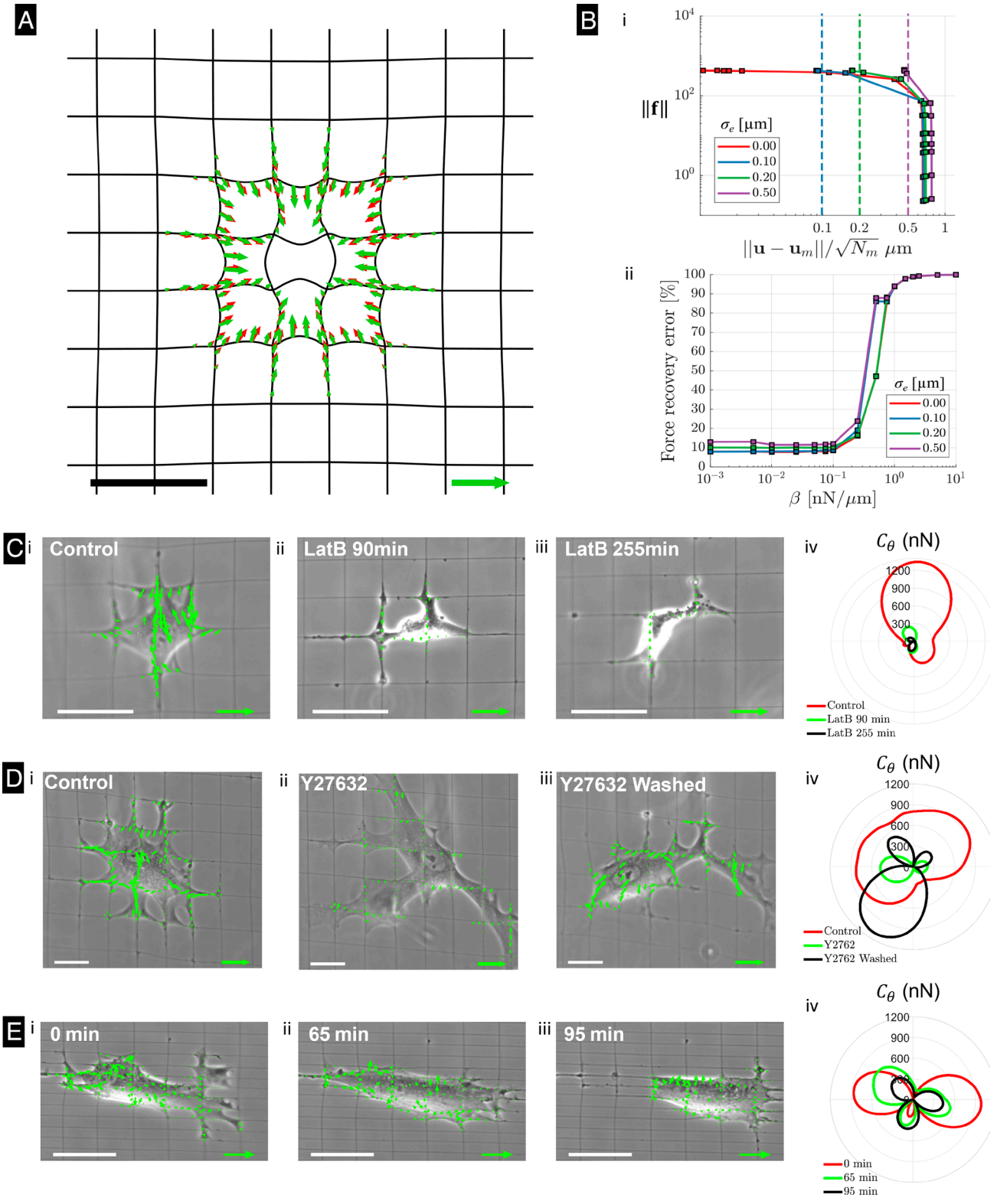

Fig. 4. Inverse formulation to estimate forces on crosshatch fiber networks. (*A*) Validation of the inverse formulation with a representative radial contractile force pattern (red arrows) generating the displacements u_m at grid intersections. The inverse problem is solved using $\mathbf{u}_m$ with zero-mean Gaussian noise of SD σ_e. The solution obtained for a typical noise strength $\sigma_e = 0.2$ μm is shown with green arrows. (*B*) Analysis of the validation example in (*A*) for different σ_e. (*i*) The L-curves showing the magnitude of the force pattern $|\,|\mathbf{f}|\,|$ as a function of the displacement matching error $|\,|\mathbf{u} - \mathbf{u}_m|\,|$ normalized by the number of measured nodes N_m for a range of regularization parameter β from 10 to 10^{-3} nN/μm. (*ii*) Recovery of forces as a function of β for different σ_e. The forces are compared after summing up within a patch of 20 μm radius (*SI Appendix, Note 5*). (*C*) Line tension map of the cell (*i*) under control condition, presence of Latrunculin B (actin inhibitor) after (*ii*) 90 min, and (*iii*) 255 min. (*iv*) Force polarity maps capturing the orientational distribution of cellular forces. (*D*) Line tension map of the cell (*i*) under control condition, (*ii*) in the presence of Y27632 drug (ROCK inhibitor), and (*iii*) after drug wash-off showing recovered contractility. (*iv*) Force polarity maps for cases *i–iii*. (*E*) *i–iii*. Line tension map of cells migrating in aligned morphology on rectangular crosshatch fibers tracked over tens of minutes. (*iv*) Force polarity maps capturing the horizontal alignment of cellular forces. The force measurements in (*C–E*) depict a single representative cell; similar results were observed in multiple cells (N = 3) across three independent experiments. Green tension scale arrow: (*A*) 25 mN/m, (*C–E*) 35 mN/m. Black/White scale bars: (*A* and *C–E*) 50 μm.

(green arrows, Fig. 4*A*) recovered force patterns with less than 10% error (Fig. 4 *B*, *ii*), where the forces are compared after summing within a circular patch of 20 μm radius. Averaged measurements of the force patterns (overall contractility C, see *Materials and Methods*) were recovered with even higher accuracy than pointwise measurements (*SI Appendix*, *Note* 5). Note that we define contractility C as the scalar sum of contractile force magnitudes across the cell–matrix interface, reflecting the overall magnitude of cellular force generation. This metric is particularly useful for comparing cells across different conditions or time points, as it integrates a complex traction pattern into a single representative value.

A regularization parameter β (i.e., parameter to penalize large, unphysical forces in the inverse solution) was chosen based on an L-curve (Fig. 4 *B*, *i*) of reconstructed force magnitude $||\mathbf{f}||$ versus normalized matching errors for a range of β values. Note that the L-curve method was used to determine the optimal regularization parameter β in our inverse mechanics formulation. The L-curve plots the norm of the solution ($||\mathbf{f}||$) against the norm of the residuals, balancing model complexity and fitting accuracy. The inflection point on this curve represents an optimal tradeoff between overfitting and underfitting, ensuring stable and physically meaningful force estimates (58, 59).

Although a typical L-curve displays a sharp increase in $||\mathbf{f}||$ as β approaches zero because of overfitting the solution to noise, this was absent in our L-curves because the image-based fitting term constrains crosshatch fiber network deformations to the fluorescent fiber shapes. The level of noise σ_e in the measured nodal displacements was relatively low (vertical dotted lines, Fig. 4 *B*, *i*). The inverse solver reduced normalized matching errors within this noise level (see *SI Appendix*, *Note* 5 for detailed analysis and more validation examples).

We applied these validated inverse methods to estimate forces exerted by cells migrating over crosshatch fiber networks. Phase contrast images were interpreted using our cGAN (Fig. 3) to generate a corresponding fluorescent image to calculate nodal deformations required for calculating cell forces (*SI Appendix,* Figs. S9 and S10). Estimated nodal forces scaled with the length of finite elements (FEs) used to discretize the nanofibers and reported as line tensions (force per unit element length in mN/m, *SI Appendix,* Fig. S10*C*). Line tensions in the range of 5 to 25 mN/m were observed, which for a representative 10 μm adhesion patch on fibers results in 50 to 250 nN force, in agreement with other reports for cells on fibers using Nanonet Force Microscopy (NFM) (9, 18, 60–62), and on the same order as forces per adhesion patch for cells on soft gels [2 to 50 nN (63–65)], fibrous networks [100 to 400 nN (18, 28, 61, 66)], and micropost arrays [1 to 80 nN (63, 67–69)]. Force polarity maps of the contractility C_θ (*SI Appendix,* Fig. S10*D* and *Materials and Methods*) showed spatial organization of cellular contractility.

Cellular Contractility during Dynamic ECM Interactions. To verify our method, we tested it in several biologically relevant scenarios. First, we verified that DLFM could detect dynamic changes in cell forces when we added drugs that target the cell's force-generating machinery. When we disrupted the cell's internal scaffolding using Latrunculin B, forces decreased as expected (Fig. 4*C* and Movie M6). Similarly, when we inhibited ROCK (Rho-associated kinase, a key regulator of cell contraction) using Y-27632, forces dropped within 30 min (Fig. 4 *D*, *i* and *ii* and Movie M7). When we removed Y-27632, cells recovered and restored their original force patterns and magnitudes (Fig. 4 *D*, *iii* and *iv*). Notably, unlike the peripheral force localization typically seen in 2D environments (49), we observed that in fibrous ECMs, cells consistently generated contractile forces both at the periphery and at locations far from the cell boundary (Fig. 4 *C*–*E* and *SI Appendix,* Fig. S10*C*).

Next, we inquired how contractility varied as cells migrated and changed shapes. Previously, we demonstrated that the spacing of fibers in crosshatch fiber networks controls cell shapes and migration direction (30, 70). On rectangular (25 μm × 8 μm) grids (Fig. 4*E* and Movie M8), cells elongated and applied forces that were mainly concentrated at their leading and trailing ends (Fig. 4 *E*, *i*–*iii*), with forces transverse to the fibers lower than those parallel to the fibers (Fig. 4 *E*, *iv*), as expected for polarized cell migration (71, 72). These results confirm that DLFM is capable of capturing both rapid and gradual changes in cell-generated forces in response to biochemical perturbations and cell dynamics, demonstrating the ability of this label-free tool to study force modulation during diverse cellular processes in real time.

Tension Anisotropy Regulates Cellular Contractility. Cells in living tissues are exposed to mechanical signals from their ECM, including tension generated through cell–ECM interactions. However, this tension is not always equal in all directions. In many physiological contexts, cells experience tension anisotropy, where the magnitude of tension differs between directions. This can result from several factors, including anisotropic ECM architecture (e.g., aligned fibers with directional stiffness) or anisotropic cellular contractility (e.g., elongated cells contracting preferentially along their long axis). We recently revealed that this anisotropy of tension, rather than tension magnitude alone, is a dominant regulator of fibroblast activation and contractility, surpassing the well-established influence of ECM stiffness (31).

To investigate this phenomenon dynamically and in real time, we used our DLFM, which allows noninvasive, real-time mapping of cellular contractile forces. We measured how cell-generated forces changed as hMSCs migrated between regions of the ECM that varied in fiber architecture, but not in fiber material properties. Specifically, we designed ECMs with adjacent regions of square (30 μm × 30 μm) and rectangular (30 μm × 15 μm) crosshatch fiber grids (Fig. 5 *A* and *C*).

On square, isotropic grids, cells generated contractile forces primarily along their migration direction (Fig. 5*C*). Because the number of fibers, and thus the stiffness, was equal in both directions on the square grids, the anisotropic contractility of cells resulted in high tension anisotropy; that is, they experienced greater tension along their axis of contraction (vertical direction). However, as cells migrated vertically into the adjacent rectangular region, where the number of horizontal fibers (and stiffness in that direction) was higher, the anisotropy of the stress field experienced by cells decreased, even though the overall ECM stiffness increased.

Our theoretical model predicted that this reduction in tension anisotropy, despite the increase in overall stiffness, would lead to a decrease in cell contractility, challenging the traditional assumption that higher stiffness always promotes stronger contractile forces (Fig. 5*B*). DLFM measurements confirmed this prediction: As cells transitioned from the square to rectangular region, their contractile forces significantly dropped (Fig. 5*C*, Movie M9, and *SI Appendix,* Fig. S11), despite keeping the same spreading area. The contractility of hMSCs was on the order of values reported on PDMS micropost arrays [1,000 to 5,000 nN, depending on cell area (29, 63)] and polyacrylamide gels [~600 to 6,000 nN (73, 74), depending on substrate stiffness].

These findings show tension anisotropy as a key regulator of cellular contractility, with effects that can outweigh the influence of ECM stiffness alone. Our study demonstrates how DLFM enables real-time interrogation of dynamic force responses as cells migrate

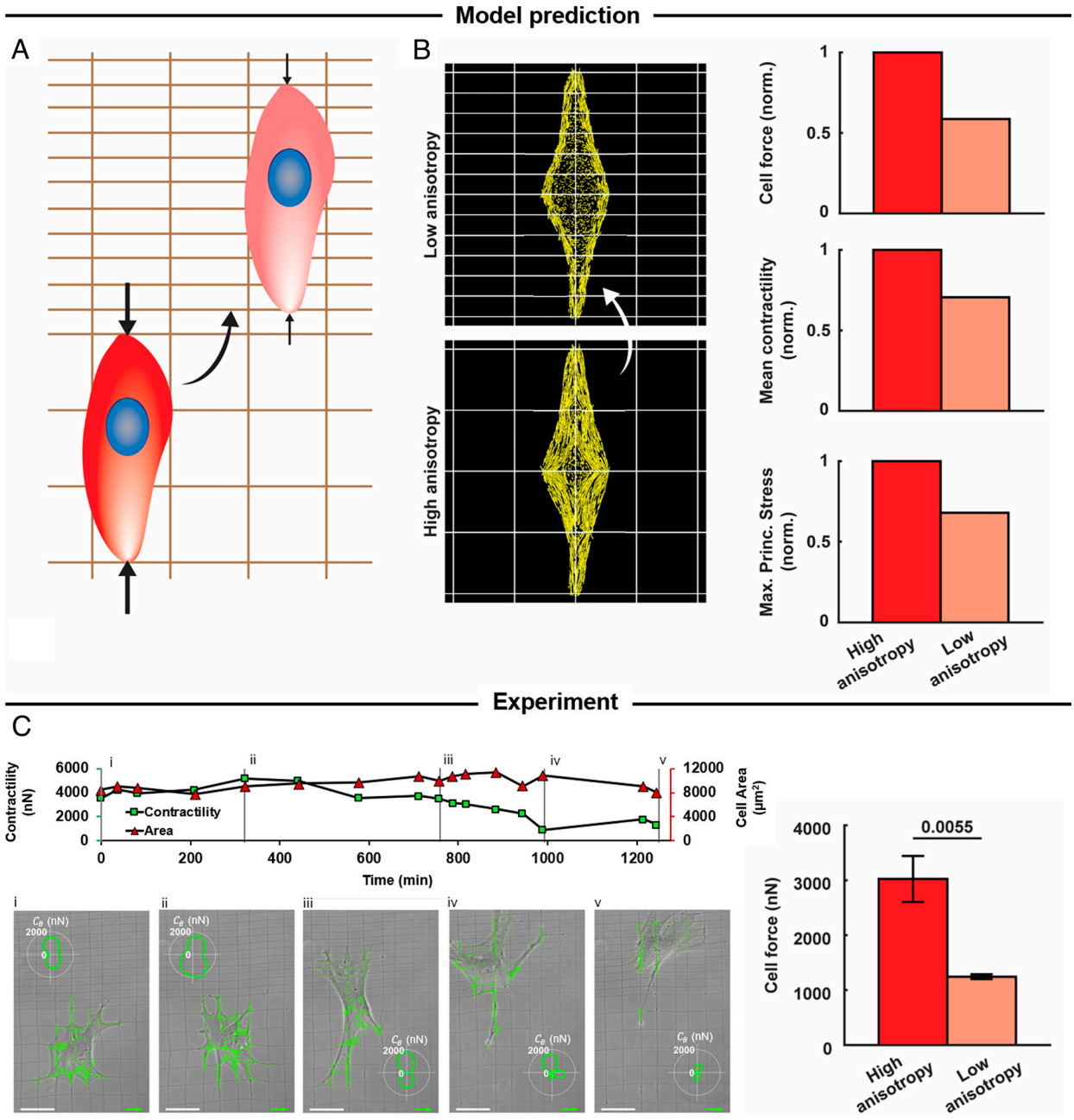

Fig. 5. Tension anisotropy regulates cellular contractility independent of ECM stiffness. (*A*) Schematic of the experimental setup showing adjacent square and rectangular fibrous ECM regions designed to modulate tension anisotropy. (*B*) The model predicts that a reduction in tension anisotropy, caused by increased stiffness perpendicular to the direction of cell contraction, leads to reduced cellular contractility, despite increased overall ECM stiffness. Yellow vectors in our simulations depict the magnitude and direction of maximum principal stress in the cytoskeleton. (*C*) DLFM measurements of hMSC contractile forces during migration from the square to rectangular region. Force polarity maps C_θ (*Insets*) show the changes in the magnitude and polarity of forces generated by cells. Cells on square grids generated higher contractile forces along their elongation (vertical) direction. As cells transitioned to the rectangular region, contractile forces significantly decreased despite no change in cell spreading area. These findings reveal that tension anisotropy, not ECM stiffness alone, governs cell contractility and highlights DLFM's ability to dynamically track force modulation in response to spatial changes in ECM architecture. n = 4. Green tension scale arrow: 35 mN/m. (White scale bar: 50 μm.)

through heterogeneous environments, offering a powerful tool to uncover the mechanical principles governing cell behavior.

Cellular Contractility during Cell–Cell Interaction and Differentiation. Cells in vivo often exist within multicellular assemblies where interactions with neighboring cells may also modulate mechanical behavior. To investigate how cell–cell interactions impact force generation, we used DLFM to monitor contractile forces in cells migrating in close proximity. We observed that as cells approached and interacted with neighboring cells, their contractile forces significantly changed, with individual cells exhibiting dynamic fluctuations in force magnitude during shape changes and migration cycles (Fig. 6*A* and Movie M10). These results demonstrate that DLFM effectively captures real-time changes in cellular contractility associated with intercellular interactions.

Finally, we show how contractility affects stem cell differentiation in compliant fibrous environments. Stem cell fate is well known to be influenced by matrix elasticity (75) and mechanical tractions (63, 76, 77). However, the evolution of tractions during differentiation on a compliant fibrous ECM has yet to be reported. hMSCs treated with adipogenic differentiation medium for nine days (red box, Fig. 6 *B*, *i*) exhibited a general reduction in contractility over time

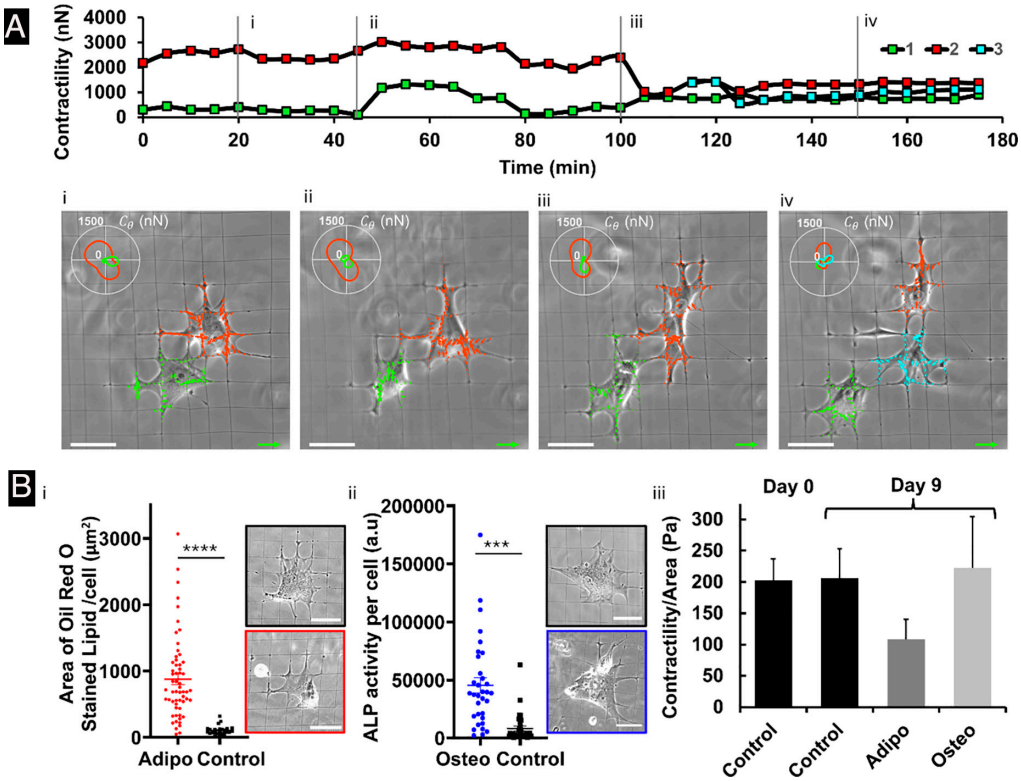

Fig. 6. Forces in cell interactions and stem cell differentiation. (*A*) Time evolution of contractility of two interacting cells and line tension maps for selected frames i-iv. Force polarity maps C_θ (*Insets*) depict the evolution of the force patterns of interacting cells along the direction of respective cell motion. The force measurements shown in (*A*) represent a single illustrative case of cell–cell interaction; however, similar trends were consistently observed across multiple cells in at least three independent experiments, demonstrating that as cells approached and interacted with neighboring cells, their contractile forces changed significantly, with individual cells exhibiting dynamic fluctuations in force magnitude during shape remodeling and migration cycles. Green tension scale arrow: 35 mN/m. (White scale bar: 50 μm.) (*B*) *i*. The total area covered by Oil Red O stained lipid droplets quantified for cells treated with adipogenic medium vs growth medium (control) confirms adipogenic differentiation. n = 58 (N = 5) for Adipogenic, n = 25 (N = 2) for Control. The image in the black box represents a cell on Day 0, and the image in the red box represents a cell on Day 9. *ii*. ALP activity of cells in osteogenic medium vs. growth medium (control) expressed in arbitrary units indicates osteogenic differentiation. n = 33 (N = 4) for Osteogenic, n = 32 (N = 2) for Control. The image in the black box represents a cell on Day 0, and the image in the blue box represents a cell on Day 9. *iii*. Cells in the growth medium (control) maintain contractility magnitudes over 9 d. Cells undergoing adipogenic differentiation exhibit lower contractility than those in growth medium (control) and those undergoing osteogenic differentiation. n = 15 (N = 2) for Control Day-0, n = 10 (N = 5) for Adipogenic, n = 6 (N = 4) for Osteogenic and Control Day-9. n = number of cells, N = number of independent samples (2 sets of independent experiments were performed for all the data). (White scale bar: 50 μm.)

(though statistically insignificant), whereas hMSCs treated with osteogenic differentiation medium for the same duration (blue box, Fig. 6 *B*, *ii*) showed a general increase in contractility. Both responses were evaluated relative to control hMSCs maintained in growth medium for nine days (Fig. 6 *B*, *iii*). We confirmed differentiation by staining for lipid droplets (adipogenic differentiation) using Oil Red (Fig. 6 *B*, *i* and *SI Appendix*, Fig. S12) and alkaline phosphatase activity (ALP, osteogenic differentiation, Fig. 6 *B*, *ii* and *SI Appendix*, Fig. S13). Results demonstrate our platform's robustness to estimate single cell contractility across a range of biological conditions, including cell–cell interactions, and differentiation.

Discussion

We present DLFM for measuring forces in live cells as they migrate on deformable networks, as would be expected in vivo. A key advantage of our approach is that it enables us to determine forces without chemically paralyzing cells, a requirement of traditional force measurement methods (24, 64, 78). Furthermore, the forces we measure and the resulting displacement field within the ECM align well with previous studies using other methods, validating our approach (10, 29, 61, 65, 66, 76, 79, 73, 80).

Our findings reveal that cells in fibrous environments operate under fundamentally different mechanical principles than those established from decades of studies on flat substrates. The finding that tension anisotropy overrides ECM stiffness in regulating the contractility of migrating cells challenges a central dogma of mechanobiology and has fascinating implications for understanding cell behavior in health and disease.

Tension Anisotropy as a Master Regulator of Behavior in Migrating Cells. DLFM-enabled observation that cells significantly reduce their contractile forces when migrating into a less anisotropic stress field, despite encountering increased stiffness, represents a paradigm shift in mechanobiology. This finding suggests explanations for several longstanding puzzles, such as why wound healing proceeds differently in tissues with oriented versus random collagen, and why certain cancers preferentially invade along aligned fiber tracks (81, 82). Results suggest that cells integrate directional mechanical information more sensitively than absolute stiffness values. This makes biological sense: In vivo, cells rarely encounter uniform mechanical environments, instead navigating landscapes where mechanical properties vary directionally due to ECM organization, neighboring cells, and tissue boundaries. The ability to sense and respond to tension anisotropy may therefore be more physiologically relevant than responding to isotropic stiffness changes.

Interior Focal Adhesions Redefine Cell–Matrix Interactions. The formation of force-generating adhesions throughout the cell body, rather than exclusively at the periphery, is a feature of how cells

anchor themselves in 3D environments (83, 84). Our combined experimental and computational approach revealed that out-of-plane force components, unique to fibrous geometries, stabilize these interior adhesions. This mechanism might contribute to ways that cells maintain mechanical integrity while navigating discontinuous spaces in ECM-mimicking fibrous networks, a challenge that does not exist on continuous 2D substrates.

Force Oscillations Encode Cellular Decisions. The dramatic force fluctuations we observed, with up to 10-fold changes during migration, reveal a previously hidden dynamic landscape of cell mechanics. The distinct temporal signatures during adipogenic versus osteogenic differentiation suggest that mechanical forces may contribute to cell fate decisions. The ability to capture these dynamics in real-time without disrupting cells through labeling or chemical treatments was crucial. Previous endpoint measurements would have averaged these oscillations, missing the rich temporal information. Our findings suggest that the magnitude of force at any single time point may be less informative than the pattern of force evolution over time, analogous to how dynamic transcriptional patterns, rather than static expression levels, often control cell fate.

Implications for Human Health. These findings have relevance for multiple areas of medicine. From the perspective of *cancer metastasis,* the dominance of tension anisotropy over stiffness may explain why cancer cells can invade efficiently along aligned collagen fibers even when the overall tissue is soft (85), which would suggest alternate therapeutic strategies focused on disrupting directional mechanical cues. From the perspective of *tissue engineering*, results suggest that controlling mechanical anisotropy may be equally or more important than matching tissue stiffness when guiding cell behavior and tissue regeneration (31). Similarly, for *stem cell therapy,* the mechanical signatures of differentiation we identified could enable noninvasive monitoring of stem cell fate in real time (86, 87). For *fibrotic diseases,* which often involve aberrant ECM alignment, understanding how tension anisotropy drives cell behavior could reveal why some fibrotic processes are self-reinforcing and suggest interventions to break these mechanical feedback loops (88).

Conclusions

The technical advancement from our work entails mapping deformable networks to a high precision using machine learning. This allowed us to watch living cells pull on their fibrous surroundings in real time, thus uncovering mechanical principles that govern cell behavior in tissue-like environments. Three key findings emerge from this work. First, tension anisotropy, not stiffness alone, controls how much force cells generate. This finding overturns the prevailing view that stiffer always means stronger when it comes to cellular forces and suggests that the directionality of mechanical signals may be the primary factor organizing cell behavior in aligned tissues. Second, cells in fibrous environments can form and maintain force-generating adhesions throughout their body by utilizing out-of-plane mechanical components unavailable on flat surfaces. This finding resolves the long-standing paradox of how interior focal adhesions remain stable without peripheral shear forces. Third, cellular forces oscillate dramatically during migration, interaction, and differentiation, with temporal patterns that predict cell fate and behavior. These dynamics, invisible to traditional endpoint measurements, reveal that force generation is not a steady state but a dynamic process encoding cellular decisions.

Together, these findings suggest principles governing how cells navigate the fibrous architecture of real tissues. In the body's fibrous landscapes, cells follow different rules: They sense directionality over magnitude, anchor throughout rather than just at edges, and generate dynamic rather than steady forces. Broadly, our results demonstrate how a methodological innovation that preserves natural cell behavior can reveal biological principles invisible to traditional approaches. DLFM opens a window into the mechanical feedback between cells and their environment.

Materials and Methods

Crosshatch Fiber Network Manufacturing. Suspended orthogonal fiber networks were generated without electrospinning using "Spinneret-based tuned engineered polymers" (STEP) (89–92). Briefly, nonelectrospun ~250 nm diameter polystyrene (Scientific Polymer Products, Ontario, NY) fibers dissolved in xylene solution (Thermo Fisher Scientific, Waltham, MA) were suspended in two orthogonal layers with defined fiber spacings, typically a 25 × 25 μm square grid or a 25 × 5–8 μm rectangular grid. For GAN training dataset generation, fibers were immersed in 4 μg/mL rhodamine-tagged fibronectin (Cytoskeleton Inc., CO).

Cell Culture, Staining, Imaging, and Quantification of Focal Adhesion Spatial Distribution. Human mesenchymal stem cells (hMSCs, Lonza) were cultured on fiber scaffolds in 5% CO_2 at 37 °C. To quantify the spatial distribution of focal adhesions, we first identified all focal adhesion clusters with an area ≥3 μm^2, following established criteria (93). See *SI Appendix, Note 6* for details on cell culture, immunostaining, differentiation media composition, protocols for Oil Red O, ALP staining, analysis of the obtained RGB images, and focal adhesion quantification.

Phase to Fluorescent Image Translation Using Pix2pix. We used a pix2pix GAN model to translate the phase contrast images to fluorescent images. Details of the pix2pix model are provided in *SI Appendix, Note 3*. Our pix2pix model was trained on a pristine phase and fluorescent image pair set (*SI Appendix, Note 3*).

Node Detection and Tracking. We used *RetinaNet* to detect grid intersections from the synthetically generated fluorescent images. We further developed a bidirectional tracking algorithm to recover nodes that the RetinaNet did not detect. Additional details of *RetinaNet* are provided in *SI Appendix, Note 3*.

FE-Based Inverse Formulation. We developed a FE–based inverse formulation to infer cellular traction forces on nanofiber networks. Nanofibers are modeled as pretensed corotational beams (94), and the inverse problem is posed as a regularized minimization of the mismatch between measured and simulated deformations. The objective combines nodal displacement errors, fiber shape alignment in artificial fluorescence images (95, 96), and a force-magnitude based regularization term. Minimization is performed using the Broyden–Fletcher–Goldfarb–Shanno algorithm (97) with gradients obtained using the adjoint-set method (98, 99, 100). The detailed formulation and validation are provided in *SI Appendix, Note 5*.

Contractility and Force Polarity Maps. To quantify the force patterns, we computed the overall cell contractility by summing up the component of forces directed toward the epicenter of the force pattern. We also assessed the orientational organization of the force patterns by calculating the angular distribution of contractility, which are visualized as force polarity maps (Fig. 4 *C–E*, *iv*) to reveal preferential alignment of contractile forces. The details are described in *SI Appendix, Note 4*.

Cell Model. We used a 3D finite elemental model of the cellular cytoskeleton (26, 46, 101) (details in *SI Appendix, Notes* 1and 2) as a continuous structure composed of i) the myosin molecular motors, ii) the actin filament network, and iii) the microtubule network. Focal adhesions are modeled as a thin, initially soft layer, which undergoes local stiffening when tensile forces at a particular location exceed a specific threshold.

Our simulations imposed symmetry about the X-Y plane, consistent with our experimental findings that cells wrap around fibers (102, 103, 104). This wrapping results in nearly symmetrical cytoskeletal distribution above and below the fiber network, leading to out-of-plane contractility that generated an almost symmetrical stress field about the X-Y plane. Although the magnitude of

these out-of-plane stresses can be significant, their symmetry minimized the out-of-plane deformations of fibers, consistent with our experimental observations where deformations were primarily in-plane and instances of significant nonplanar deformations were rare.

Decay of ECM Deformation Fields. We quantified ECM deformation fields using FEs simulations of nanonets and experimental data (*SI Appendix, Note 4*). Displacement magnitudes u at fiber intersections were measured as a function of the distance δ from the cell centroid to examine power-law decay of the form $u \sim \delta^{-\alpha}$, where α is the scaling exponent.

Statistical Analysis. Statistical analysis was performed using GraphPad Prism (GraphPad Software, La Jolla, CA) software. Statistical comparisons among multiple groups were performed using one-way ANOVA and Tukey's honest significant difference test. Pairwise statistical comparisons were performed using Student's *t* test. Error bars in scatter data plots indicate SD. *, **, ***, and **** represent $P < 0.05$, 0.01, 0.001, and 0.0001, respectively.

Data, Materials, and Software Availability. The code developed for DLFM as well as the FE code used for modeling cell mechanics is publicly available on GitHub at https://github.com/nain430/DLFM (105). All other data are included in the manuscript and/or supporting information.

ACKNOWLEDGMENTS. S.K., A.K., and A.S.N. acknowledge funding support from the NSF (Grant No. 2107332). A.S.N. acknowledges partial funding from the NSF (Grant Nos. 2422340 and 2119949) and the National Institute of Health (1R01 HL162822-01A1). A.S.N. acknowledges the Institute for Critical Technology and Applied Science and Macromolecules Innovative Institute at Virginia Tech for supporting this study. F.A. acknowledges startup funding provided by New Jersey Institute of Technology. G.M.G. acknowledges support from the NIH (grants R01DK131177, R01AR077793, and R01HL159094); the NSF through grants CMMI 1548571 (the NSF Science and Technology Center for Engineering Mechanobiology) and OIA-2219142; and the Human Frontier Science Program (grant HFSP–RGP016/2024, https://doi.org/10.52044/HFSP.RGP0162024.pc.gr.194164). A.P. and A.S.N. thank Prof. Dai Fei Elmer Ker for insightful discussions on differentiation experiments.

Author affiliations: [a]Department of Mechanical Engineering, Virginia Tech, Blacksburg, VA 24061; [b]Department of Computer Science, Virginia Tech, Blacksburg, VA 24061; [c]Department of Mechanical and Industrial Engineering, New Jersey Institute of Technology, Newark, NJ 07102; [d]National Science Foundation Science and Technology Center for Engineering Mechanobiology, Washington University in St. Louis, St. Louis, MO 63130; [e]Department of Mechanical Engineering and Materials Science, Washington University in St. Louis, St. Louis, MO 63130; and [f]Center of Soft Matter and Biological Physics, Virginia Tech, Blacksburg, VA 24061

1. D. A. Lauffenburger, A. F. Horwitz, Cell migration: A physically integrated molecular process. *Cell* **84**, 359–369 (1996).
2. R. Ananthakrishnan, A. Ehrlicher, The forces behind cell movement. *Int. J. Biol. Sci.* **3**, 303–317 (2007).
3. F. Alisafaei, X. Chen, T. Leahy, P. A. Janmey, V. B. Shenoy, Long-range mechanical signaling in biological systems. *Soft Matter* **17**, 241–253 (2021).
4. B. M. Baker *et al.*, Cell-mediated fibre recruitment drives extracellular matrix mechanosensing in engineered fibrillar microenvironments. *Nat. Mater.* **14**, 1262–1268 (2015).
5. X. Peng, Y. Huang, G. M. Genin, The fibrous character of pericellular matrix mediates cell mechanotransduction. *J. Mech. Phys. Solids* **180**, 105423 (2023).
6. X. Cao *et al.*, Multiscale model predicts increasing focal adhesion size with decreasing stiffness in fibrous matrices. *Proc. Natl. Acad. Sci. U.S.A.* **114**, E4549–E4555 (2017).
7. S. Coyle *et al.*, Cell alignment modulated by surface nano-topography–Roles of cell-matrix and cell-cell interactions. *Acta Biomater.* **142**, 149–159 (2022).
8. C. E. Chan, D. J. Odde, Traction dynamics of filopodia on compliant substrates. *Science* **322**, 1687–1691 (2008).
9. A. Padhi *et al.*, Force-exerting perpendicular lateral protrusions in fibroblastic cell contraction. *Commun. Biol.* **3**, 390 (2020).
10. M. S. Hall *et al.*, Fibrous nonlinear elasticity enables positive mechanical feedback between cells and ECMs. *Proc. Natl. Acad. Sci. U.S.A.* **113**, 14043–14048 (2016).
11. R. Malik, P. I. Lelkes, E. Cukierman, Biomechanical and biochemical remodeling of stromal extracellular matrix in cancer. *Trends Biotechnol.* **33**, 230–236 (2015).
12. T. R. Cox, J. T. Erler, Remodeling and homeostasis of the extracellular matrix: Implications for fibrotic diseases and cancer. *Dis. Model. Mech.* **4**, 165–178 (2011).
13. M. Larsen, V. V. Artym, J. A. Green, K. M. Yamada, The matrix reorganized: Extracellular matrix remodeling and integrin signaling. *Curr. Opin. Cell Biol.* **18**, 463–471 (2006).
14. S. Van Helvert, C. Storm, P. Friedl, Mechanoreciprocity in cell migration. *Nat. Cell Biol.* **20**, 8–20 (2018).
15. P. H. Wu, A. Giri, S. X. Sun, D. Wirtz, Three-dimensional cell migration does not follow a random walk. *Proc. Natl. Acad. Sci. U.S.A.* **111**, 3949–3954 (2014).
16. R. C. Picu, S. Deogekar, M. R. Islam, Poisson's contraction and fiber kinematics in tissue: Insight from collagen network simulations. *J. Biomech. Eng.* **140**, 021002 (2018).
17. K. Sheets, S. Wunsch, C. Ng, A. S. Nain, Shape-dependent cell migration and focal adhesion organization on suspended and aligned nanofiber scaffolds. *Acta Biomater.* **9**, 7169–7177 (2013).
18. A. Jana *et al.*, Sculpting rupture-free nuclear shapes in fibrous environments. *Adv. Sci.* **9**, 2203011 (2022).
19. M. Dembo, Y. L. Wang, Stresses at the cell-to-substrate interface during locomotion of fibroblasts. *Biophys. J.* **76**, 2307–2316 (1999).
20. N. Q. Balaban *et al.*, Force and focal adhesion assembly: A close relationship studied using elastic micropatterned substrates. *Nat. Cell Biol.* **3**, 466–472 (2001).
21. A. Malandrino, X. Trepat, R. D. Kamm, M. Mak, Dynamic filopodial forces induce accumulation, damage, and plastic remodeling of 3D extracellular matrices. *PLoS Comput. Biol.* **15**, 1–26 (2019).
22. H. Colin-York, M. Fritzsche, The future of traction force microscopy. *Curr. Opin. Biomed. Eng.* **5**, 1–5 (2018).
23. H. Colin-York *et al.*, Super-resolved traction force microscopy (STFM). *Nano Lett.* **16**, 2633–2638 (2016).
24. Y.-L. Wang, Y.-C. Lin, Traction force microscopy by deep learning. *Biophys. J.* **120**, 3079–3090 (2021).
25. W. R. Legant *et al.*, Measurement of mechanical tractions exerted by cells in three-dimensional matrices. *Nat. Methods* **7**, 969–971 (2010).
26. D. Shakiba *et al.*, The balance between actomyosin contractility and microtubule polymerization regulates hierarchical protrusions that govern efficient fibroblast-collagen interactions. *ACS Nano* **14**, 7868–7879 (2020).
27. A. Padhi *et al.*, Bioenergetics underlying single-cell migration on aligned nanofiber scaffolds. *Am. J. Physiol. Cell Physiol.* **318**, C476–C485 (2020).
28. K. Sheets, J. Wang, W. Zhao, R. Kapania, A. S. Nain, Nanonet force microscopy for measuring cell forces. *Biophys. J.* **111**, 197–207 (2016).
29. X. Xue, X. Hong, Z. Li, C. X. Deng, J. Fu, Acoustic tweezing cytometry enhances osteogenesis of human mesenchymal stem cells through cytoskeletal contractility and YAP activation. *Biomaterials* **134**, 22–30 (2017).
30. A. Jana *et al.*, Crosshatch nanofiber networks of tunable interfiber spacing induce plasticity in cell migration and cytoskeletal response. *FASEB J.* **33**, 10618–10632 (2019).
31. F. Alisafaei *et al.*, Tension anisotropy drives fibroblast phenotypic transition by self-reinforcing cell–extracellular matrix mechanical feedback. *Nat. Mater.* **24**, 955–965 (2025).
32. H. Wang *et al.*, Deep learning enables cross-modality super-resolution in fluorescence microscopy. *Nat. Methods* **16**, 103–110 (2019).
33. M. Jemielita, M. J. Taormina, A. Delaurier, C. B. Kimmel, R. Parthasarathy, Comparing phototoxicity during the development of a zebrafish craniofacial bone using confocal and light sheet fluorescence microscopy techniques. *J. Biophotonics* **6**, 920–928 (2013).
34. R. Dixit, R. Cyr, Cell damage and reactive oxygen species production induced by fluorescence microscopy: Effect on mitosis and guidelines for non-invasive fluorescence microscopy. *Plant J.* **36**, 280–290 (2003).
35. J. Hayashida, K. Nishimura, R. Bise, "MPM: Joint representation of motion and position map for cell tracking" in *Proceedings of the IEEE Conference on Computer Vision and Pattern Recognition*, E. Mortensen, Ed. (IEEE, 2020), pp. 3822–3831, 10.1109/CVPR42600.2020.00388.
36. E. Moen *et al.*, Deep learning for cellular image analysis. *Nat. Methods* **16**, 1233–1246 (2019).
37. C. Wen *et al.*, 3DeeCellTracker, a deep learning-based pipeline for segmenting and tracking cells in 3D time lapse images. *Elife* **10**, e59187 (2021).
38. H. Wang *et al.*, Biological image analysis using deep learning-based methods: Literature review. *Digit. Med.* **4**, 157–165 (2018).
39. S. T. H. Shah, X. Xuezhi, Traditional and modern strategies for optical flow: An investigation. *SN Appl. Sci.* **3**, 289 (2021).
40. T. N. A. Nguyen, J. Cai, J. Zhang, J. Zheng, Robust Interactive Image Segmentation Using Convex Active Contours. *IEEE Trans. Image Process.* **21**, 3734–3743 (2012).
41. A. Creswell *et al.*, Generative adversarial networks: An overview. *IEEE Signal Process. Mag.* **35**, 53–65 (2018).
42. A. Kadambi, C. de Melo, C.-J. Hsieh, M. Srivastava, S. Soatto, Incorporating physics into data-driven computer vision. *Nat. Mach. Intell.* **5**, 572–580 (2023).
43. L. Fang *et al.*, Deep learning-based point-scanning super-resolution imaging. *Nat. Methods* **18**, 406–416 (2021).
44. E. M. Christiansen *et al.*, In silico labeling: Predicting fluorescent labels in unlabeled images. *Cell* **173**, 792–803.e19 (2018).
45. C. Ounkomol, S. Seshamani, M. M. Maleckar, F. Collman, G. R. Johnson, Label-free prediction of three-dimensional fluorescence images from transmitted-light microscopy. *Nat. Methods* **15**, 917–920 (2018).
46. F. Alisafaei, D. S. Jokhun, G. V. Shivashankar, V. B. Shenoy, Regulation of nuclear architecture, mechanics, and nucleocytoplasmic shuttling of epigenetic factors by cell geometric constraints. *Proc. Natl. Acad. Sci. U.S.A.* **116**, 13200–13209 (2019).
47. V. B. Shenoy, H. Wang, X. Wang, A chemo-mechanical free-energy-based approach to model durotaxis and extracellular stiffness-dependent contraction and polarization of cells. *Interface Focus* **6**, 20150067 (2016).
48. M. Versaevel, T. Grevesse, S. Gabriele, Spatial coordination between cell and nuclear shape within micropatterned endothelial cells. *Nat. Commun.* **3**, 671 (2012).
49. P. W. Oakes, S. Banerjee, M. C. Marchetti, M. L. Gardel, Geometry regulates traction stresses in adherent cells. *Biophys. J.* **107**, 825–833 (2014).
50. W. R. Legant *et al.*, Multidimensional traction force microscopy reveals out-of-plane rotational moments about focal adhesions. *Proc. Natl. Acad. Sci. U.S.A.* **110**, 881–886 (2013).
51. P. Isola, J.-Y. Zhu, T. Zhou, A. A. Efros, "Image-to-image translation with conditional adversarial networks" in *Proceedings of the IEEE Conference on Computer Vision and Pattern Recognition* (2017), pp.1125–1134.
52. M. Mirza, S. Osindero, Conditional generative adversarial nets. arXiv [Preprint] (2014). https://doi.org/10.48550/arXiv.1411.1784 (Accessed 15 January 2021).
53. I. J. Goodfellow *et al.*, Generative adversarial networks. arXiv [Preprint] (2014). https://doi.org/10.48550/arXiv.1406.2661 (Accessed 15 January 2021).

54. T. Y. Lin, P. Goyal, R. Girshick, K. He, P. Dollar, Focal loss for dense object detection. *IEEE Trans. Pattern Anal. Mach. Intell.* **42**, 318–327 (2020).
55. U. S. Schwarz, J. R. D. Soiné, Traction force microscopy on soft elastic substrates: A guide to recent computational advances. *Biochim. Biophys. Acta* **1853**, 3095–3104 (2015).
56. Y. L. Han *et al.*, Cell contraction induces long-ranged stress stiffening in the extracellular matrix. *Proc. Natl. Acad. Sci. U.S.A.* **115**, 4075–4080 (2018).
57. P.-N. Tan, M. Steinbach, V. Kumar, *Introduction to Data Mining* (Pearson Education India, 2016).
58. U. S. Schwarz, J. R. D. Soiné, Traction force microscopy on soft elastic substrates: A guide to recent computational advances. *Biochim. Biophys. Acta Mol. Cell Res.* **1853**, 3095–3104 (2015).
59. P. C. Hansen, Rank-Deficient and discrete Ill-posed problems (1998). https://epubs.siam.org/doi/book/10.1137/1.9780898719697.
60. P. M. Graybill, A. Jana, R. K. Kapania, A. S. Nain, R. V. Davalos, Single cell forces after electroporation. *ACS Nano* **15**, 2554–2568 (2021).
61. A. Sarkar *et al.*, Confinement in fibrous environments positions and orients mitotic spindles. *PNAS Nexus* **4**, pgaf201 (2025).
62. A. Mukherjee *et al.*, Actin filaments couple the protrusive tips to the nucleus through the I-BAR domain protein IRSp53 during the migration of cells on 1D fibers. *Adv. Sci.* **10**, 2207368 (2023).
63. J. Fu *et al.*, Mechanical regulation of cell function with geometrically modulated elastomeric substrates. *Nat. Methods* **7**, 733–736 (2010).
64. S. J. Han, Y. Oak, A. Groisman, G. Danuser, Traction microscopy to identify force modulation in subresolution adhesions. *Nat. Methods* **12**, 653–656 (2015).
65. B. Emon *et al.*, A novel method for sensor-based quantification of single/multicellular force dynamics and stiffening in 3D matrices. *Sci. Adv.* **7**, eabf2629 (2021).
66. S. Sharma *et al.*, Mechanical cues guide the formation and patterning of 3D spheroids in fibrous environments. *PNAS Nexus* **4**, pgaf263 (2025), 10.1093/PNASNEXUS/PGAF263.
67. S. J. Han, K. S. Bielawski, L. H. Ting, M. L. Rodriguez, N. J. Sniadecki, Decoupling substrate stiffness, spread area, and micropost density: A close spatial relationship between traction forces and focal adhesions. *Biophys. J.* **103**, 640–648 (2012).
68. J. L. Tan *et al.*, Cells lying on a bed of microneedles: An approach to isolate mechanical force. *Proc. Natl. Acad. Sci. U.S.A.* **100**, 1484–1489 (2003).
69. S. Weng, Y. Shao, W. Chen, J. Fu, Mechanosensitive subcellular rheostasis drives emergent single-cell mechanical homeostasis. *Nat. Mater.* **15**, 961–967 (2016).
70. A. Mukherjee *et al.*, Quantitative biophysical metrics for rapid evaluation of ovarian cancer metastatic potential. *Mol. Biol. Cell* **33**, ar55 (2022).
71. J. Steinwachs *et al.*, Three-dimensional force microscopy of cells in biopolymer networks. *Nat. Methods* **13**, 171–176 (2016).
72. M. Lekka, K. Gnanachandran, A. Kubiak, T. Zieliński, J. Zemła, Traction force microscopy–Measuring the forces exerted by cells. *Micron* **150**, 103138 (2021).
73. A. Tijore *et al.*, Role of cytoskeletal tension in the induction of cardiomyogenic differentiation in micropatterned human mesenchymal stem cell. *Adv. Healthc. Mater.* **4**, 1399–1407 (2015).
74. W. J. Polacheck, C. S. Chen, Measuring cell-generated forces: A guide to the available tools. *Nat. Methods* **13**, 415–423 (2016).
75. A. J. Engler, S. Sen, H. L. Sweeney, D. E. Discher, Matrix elasticity directs stem cell lineage specification. *Cell* **126**, 677–689 (2006).
76. S. Abuhattum, A. Gefen, D. Weihs, Ratio of total traction force to projected cell area is preserved in differentiating adipocytes. *Integr. Biol. (Camb).* **7**, 1212–1217 (2015).
77. S. Khetan *et al.*, Degradation-mediated cellular traction directs stem cell fate in covalently crosslinked three-dimensional hydrogels. *Nat. Mater.* **12**, 458–465 (2013).
78. X. Tang, A. Tofangchi, S. V. Anand, T. A. Saif, A novel cell traction force microscopy to study multi-cellular system. *PLoS Comput. Biol.* **10**, e1003631 (2014).
79. L. A. Lautscham *et al.*, Migration in confined 3D environments is determined by a combination of adhesiveness, nuclear volume, contractility, and cell stiffness. *Biophys. J.* **109**, 900–913 (2015).
80. C. M. Kraning-Rush *et al.*, The role of the cytoskeleton in cellular force generation in 2D and 3D environments. *Phys. Biol.* **8**, 015009 (2011).
81. M. Xue, C. J. Jackson, Extracellular matrix reorganization during wound healing and its impact on abnormal scarring. *Adv. Wound Care.* **4**, 119–136 (2015).
82. P. P. Provenzano *et al.*, Collagen reorganization at the tumor-stromal interface facilitates local invasion. *BMC Med.* **4**, 38 (2006).
83. A. D. Doyle, K. M. Yamada, Mechanosensing via cell-matrix adhesions in 3D microenvironments. *Exp. Cell Res.* **343**, 60–66 (2016).
84. B. Geiger, J. P. Spatz, A. D. Bershadsky, Environmental sensing through focal adhesions. *Nat. Rev. Mol. Cell Biol.* **10**, 21–33 (2009).
85. W. Han *et al.*, Oriented collagen fibers direct tumor cell intravasation. *Proc. Natl. Acad. Sci. U.S.A.* **113**, 11208–11213 (2016).
86. M. J. Mondrinos *et al.*, Surface-directed engineering of tissue anisotropy in microphysiological models of musculoskeletal tissue. *Sci. Adv.* **7**, 9446–9458 (2021).
87. T. Popielarczyk, A. Nain, J. Barrett, Aligned nanofiber topography directs the tenogenic differentiation of mesenchymal stem cells. *Appl. Sci.* **7**, 59 (2017).
88. Y. Hong *et al.*, Cell–matrix feedback controls stretch-induced cellular memory and fibroblast activation. *Proc. Natl. Acad. Sci. U.S.A.* **122**, e2322762122 (2025).
89. A. S. Nain, M. Sitti, A. Jacobson, T. Kowalewski, C. Amon, Dry spinning based spinneret based tunable engineered parameters (STEP) technique for controlled and aligned deposition of polymeric nanofibers. *Macromol. Rapid Commun.* **30**, 1406–1412 (2009).
90. J. Wang, A. S. Nain, Suspended micro/nanofiber hierarchical biological scaffolds fabricated using non-electrospinning STEP technique. *Langmuir* **30**, 13641–13649 (2014).
91. A. S. Nain, J. Wang, Polymeric nanofibers: Isodiametric design space and methodology for depositing aligned nanofiber arrays in single and multiple layers. *Polym. J.* **45**, 695–700 (2013).
92. A. Jana *et al.*, Mitotic outcomes and errors in fibrous environments. *Proc. Natl. Acad. Sci. U.S.A.* **120**, e2120536120 (2023).
93. D.-H. Kim, D. Wirtz, Focal adhesion size uniquely predicts cell migration. *FASEB J.* **27**, 1351–1361 (2013), 10.1096/fj.12-220160.
94. R. De Borst, M. A. Crisfield, J. J. C. Remmers, C. V. Verhoosel, *Nonlinear Finite Element Analysis of Solids and Structures* (John Wiley and Sons, 2012).
95. M. Kass, A. Witkin, D. Terzopoulos, Snakes: Active contour models. *Int. J. Comput. Vis.* **1**, 321–331 (1988).
96. L. D. Cohen, On active contour models and balloons. *CVGIP Image Underst.* **53**, 211–218 (1991).
97. J. Nocedal, S. J. Wright, *Numerical Optimization* (Springer, New York, NY, 2006).
98. A. A. Oberai, N. H. Gokhale, G. R. Feijóo, Solution of inverse problems in elasticity imaging using the adjoint method. *Inverse Probl.* **19**, 297 (2003).
99. D. Song, N. Hugenberg, A. A. Oberai, Three-dimensional traction microscopy with a fiber-based constitutive model. *Comput. Methods Appl. Mech. Eng.* **357**, 112579 (2019).
100. D. Song *et al.*, Recovery of tractions exerted by single cells in three-dimensional nonlinear matrices. *J. Biomech. Eng.* **142**, 81012 (2020).
101. J. Zhang *et al.*, Nuclear mechanics within intact cells is regulated by cytoskeletal network and internal nanostructures. *Small* **16**, 1907688 (2020).
102. J. H. Faghmous *et al.*, A daily global mesoscale ocean eddy dataset from satellite altimetry. *Sci. Data* **2**, 1–16 (2015).
103. K. He *et al.*, "Masked autoencoders are scalable vision learners" in *2022 IEEE/CVF Conference on Computer Vision and Pattern Recognition (CVPR)*, K. Dana, Ed. (IEEE, 2022), pp. 15979–15988, 10.1109/CVPR52688.2022.01553.
104. A. Mukherjee, B. Behkam, A. S. Nain, Cancer cells sense fibers by coiling on them in a curvature-dependent manner. *iScience* **19**, 905–915 (2019).
105. A. Padhi *et al.*, DLFM Code. GitHub. https://github.com/nain430/DLFM. Deposited 16 July 2025.